NASA Langley Aerothermodynamic Ground Tests in Support of the Boundary Layer Transition (BOLT) Flight Experiment

Elizabeth F. Rieken*, Scott A. Berry†, Michelle L. Mason‡, and Francis A. Greene§
NASA Langley Research Center, Hampton, VA 23681

The Air Force Office of Scientific Research (AFOSR) has sponsored the Boundary Layer Transition (BOLT) Experiments to investigate hypersonic boundary layer transition on a low-curvature, concave surface with swept leading edges. This paper provides a review of aerothermodynamic ground test contributions by NASA Langley Research Center to the design of the BOLT flight experiment. Several test entries into the Langley Aerothermodynamics Laboratory 20-Inch Mach 6 Air Tunnel are discussed. Global surface heating distributions on subscale BOLT models were measured using either phosphor thermography or infrared thermography at a range of model attitudes and freestream Reynolds numbers. An initial test entry provided the first experimental measurements of transition on the BOLT geometry. A second test entry investigated the effects of distributed surface roughness along the swept leading edges. A third test entry provided an evaluation of the aeroheating environment on the aerodynamic fairings and a portion of the flight vehicle downstream of the BOLT experiment. These entries were intended to support the development and design of flight hardware and instrumentation for the BOLT flight experiment.

I. Nomenclature

H_{AW}	=	adiabatic wall surface enthalpy, J/kg
H_W	=	surface enthalpy, J/kg
H_0	=	wind tunnel total enthalpy, J/kg
H_{300K}	=	enthalpy at 300 K temperature, J/kg
h	=	convective heat transfer coefficient, kg/(m^{2}s)
h_{FR}	=	convective heat transfer coefficient based on Fay-Riddell theory, kg/(m^{2}s)
M_∞	=	freestream Mach number
L_{BOLT}	=	total length of BOLT Flight Geometry, mm

*Aerospace Engineer, Aerothermodynamics Branch, AIAA Member
†Aerospace Engineer, Aerothermodynamics Branch, AIAA Associate Fellow
‡Aerospace Engineer, Aerothermodynamics Branch, AIAA Member
§Aerospace Engineer, Aerothermodynamics Branch, AIAA Associate Fellow

q = heat transfer rate, W/m^2

Re_L = length Reynolds number

Re_∞ = freestream unit Reynolds number, 1/m

T_∞ = freestream temperature, K

U_∞ = freestream velocity, m/s

x = axial coordinate with origin at the physical nose tip, mm

y = spanwise coordinate with origin at the physical nose tip, mm

z = vertical coordinate with origin at the physical nose tip, mm

α_T = total angle of attack, the angle between the longitudinal axis and the freestream velocity vector, deg

α = angle of attack, deg

β = sideslip angle, deg

ρ_∞ = freestream density, kg/m^3

II. Introduction

The Air Force Office of Scientific Research (AFOSR) has sponsored the Boundary Layer Transition (BOLT) Experiments with an objective to investigate hypersonic boundary layer transition mechanisms on a complex geometry. Johns Hopkins University Applied Physics Laboratory (JHU/APL) is overseeing the BOLT team, which includes members from government, academia, and industry. Progressing from the Hypersonic International Flight Research Experimentation Program (HIFiRE) axisymmetric circular cone (HIFiRE-1 [1]) and nonaxisymmetric elliptical cones (HIFiRE-5A/HIFiRE-5B [2]), the BOLT geometry is a low-curvature, concave surface with swept leading edges. The BOLT Experiments are designed to use numerical prediction tools and ground-test campaigns to estimate transition on the BOLT geometry. The project will culminate in a sounding rocket flight experiment to test the prediction effort. References [3, 4] provide an overview of the BOLT flight experiment.

Figure 1 shows the forward portion of the "Flight Research Vehicle" consisting of the JHU/APL BOLT experimental payload, or "Flight Geometry", and two support modules provided by the Air Force Research Laboratory/Aerospace Systems Directorate (AFRL/RQ). The BOLT geometry features four symmetric swept leading edges and two symmetric upper and lower concave surfaces. The highly curved regions between the top and bottom surfaces are referred to as the gutters and are intended to isolate flow from each of the swept leading edges. Aft of the BOLT geometry are the AFRL/RQ Transition Support Module (TSM) and Payload Support Module (PSM) that contain the data acquisition flight computers, power for the experiment subsystems, a GPS, and an Inertial Measurement Unit (IMU). Aerodynamic fairings are attached to the rear bulkhead of the BOLT Flight Geometry to smooth transition of the Flight Geometry to the TSM. The purpose of the aerodynamic fairings is to reduce buffeting and to prevent a large flow separation at the aft

end of the BOLT Flight Geometry.

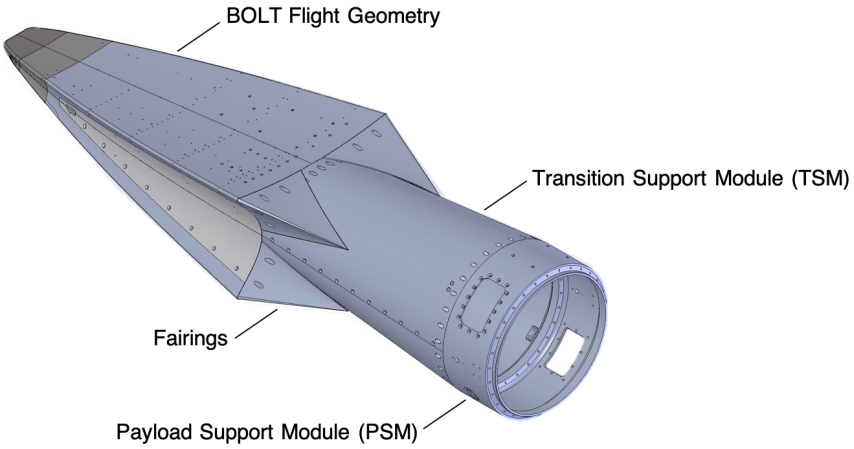


Fig. 1 BOLT Flight Geometry, aerodynamic fairings, TSM, and PSM.

This paper discusses three wind tunnel tests that were performed by the NASA Langley Research Center (LaRC) in support of the BOLT flight experiment. Aeroheating data for all tests were obtained in the NASA Langley 20-Inch Mach 6 Air Tunnel using either global phosphor thermography or infrared (IR) thermography. Descriptions are given of the facility, the wind tunnel models, the test techniques, and the data reduction and uncertainty. Global heat transfer distributions are provided for all three tests. The primary goal of these tests was to support the development and design of flight hardware and instrumentation for the BOLT flight experiment.

The BOLT effort was officially established in September 2017 with the selection of JHU/APL as the lead for design and development of the flight vehicle. The first test discussed in this paper was completed in August 2017, prior to the BOLT kick-off meeting in order to provide the project an initial set of aeroheating data based on the preliminary version of the BOLT geometry. Utilizing LaRC's phosphor thermography technique, data on a half-scale BOLT model were obtained in less than three weeks after getting the geometry from the government team that was leading the selection process and the early design. This test provided the first experimental measurements of transition on the BOLT geometry.

A second test was completed in May 2018 on a one-third-scale BOLT model. It was intended to investigate the effects of distributed surface roughness along the BOLT swept leading edges on boundary layer transition. Making use of the symmetry of the BOLT geometry, one leading edge was left smooth and the remaining three leading edges had patches of increasing roughness etched into the surface. An additional purpose of this study was to explore the use of a newer test technique under development at LaRC using IR thermogaphy on very accurately milled models built from relatively cheap resin material called PEEK (poly-ether-ether-ketone).

The third test discussed in this paper was completed in February 2019 leading up to the BOLT Critical Design Review (CDR). It was determined that aerodynamic fairings at the interface between the BOLT Flight Geometry and the TSM were necessary to reduce the occurrence of buffeting and to reduce flow separation and reattachment on the TSM.

A fast-paced wind tunnel test of a quarter-scale model encompassing the BOLT Flight Geometry, the fairings, and the TSM was run to investigate and identify any aeroheating issues on the fairings and the TSM for inclusion in the CDR proceedings. Additional analysis of these data compared heating on the TSM for the nominal vehicle reentry case with heating for off-nominal vehicle reentry cases. The heating comparison was used to evaluate thermal modeling safety margins for the prediction of temperatures on the fairings and downstream modules.

Not discussed in this paper are results from a test entry of the one-third-scale BOLT JHU/APL model (see Ref. [5]) that was completed in June and July 2018 in the NASA Langley 20-Inch Mach 6 Air Tunnel. Results were provided to JHU/APL, some of which are captured within Refs. [5] and [6]. The goals of this entry were to measure boundary layer instabilities and the effects of steps on boundary layer transition at Mach 6 on the JHU/APL subscale BOLT model. Measurements included unsteady pressures (PCB and Kulite), mean heat flux (Schmidt-Boelter), and IR thermography on the PEEK section.

III. Experimental Methods

A. Test Facility

The data in this paper were acquired in the NASA Langley 20-Inch Mach 6 Air Tunnel, which is part of the Langley Aerothermodynamics Laboratory (LAL) facilities [7]. The 20-Inch Mach 6 Air Tunnel is a conventional hypersonic blowdown facility that uses heated, dried, and filtered air as the test gas. The nominal operating pressure range is from 206.8 kPa to 3275 kPa and the maximum temperature achievable is 555.6 K. A two-dimensional, contoured nozzle is used to provide perfect-gas freestream conditions with freestream Mach numbers of 5.8 to 6.1 and unit Reynolds numbers of 1.6×10^6/m (0.5×10^6/ft) to 27.2×10^6/m (8.3×10^6/ft). The nozzle throat is 8.64-mm by 508-mm (0.34-in by 20.0-in), which then expands into the 508-mm by 521-mm (20.0-in by 20.5-in) test section. A bottom-mounted model injection system is used to insert models from a sheltered position to the tunnel centerline, which for aeroheating tests is done as quickly as possible (less than 0.5-sec traverse through the tunnel boundary layer). Run times up to 20 minutes are possible with this facility, although for the current heat transfer tests, the model was exposed to the flow for only a few seconds. Flow conditions are typically determined, based on perfect-gas calculations, from the measured reservoir pressure and temperature and the measured pitot pressure at the test section.

B. Models

The BOLT Flight Geometry is described in detail in Ref. [3] as 866-mm (34.1-in) long with a flight nose radius of 5-mm (0.197-in). The initial test at Langley was with a half-scale model (432-mm or 17.0-in long) using the phosphor thermography technique. For this technique, a slip-cast ceramic wind tunnel model was fabricated at Langley using the process outlined in Ref. [8]. Figure 2 provides a photograph of the ceramic BOLT model installed in the retracted position of the 20-Inch Mach 6 Air Tunnel.

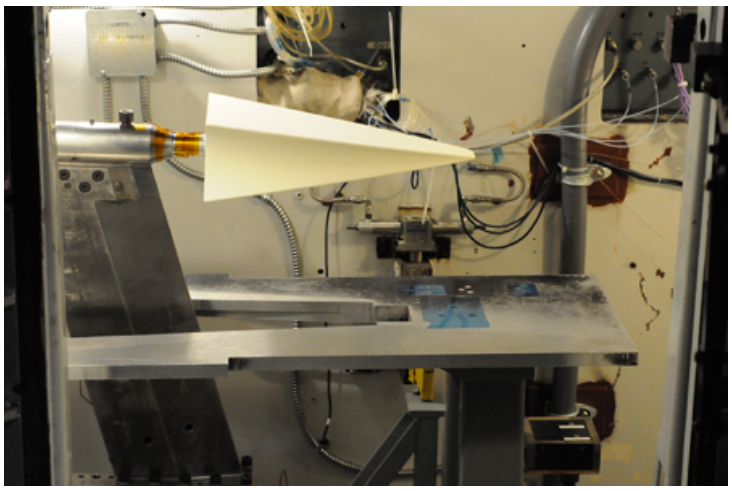


Fig. 2 Half-scale BOLT ceramic model for the preliminary transition assessment test shown in the 20-Inch Mach 6 Air Tunnel in the retracted position.

The second test was completed with a model fabricated out of PEEK for use with IR thermography. Figure 3 provides a photo of the PEEK model, including an inset photo that zooms in on a leading edge with a roughness patch etched onto the surface. The model was 305-mm (12.0-in) long, or roughly a one-third-scale model and was intended to include small patches of distributed roughness near the swept leading edges. As a rough estimate of a general build time using this approach, it is close to four months (two months to build the basic geometry using an in-house milling machine and two months to laser etch the roughness, depending on the vendor workload). From a practicality perspective, it is faster and cheaper to use the standard phosphor thermography approach, but only if well-controlled, minute surface details are not required.

The goal of the PEEK model was to investigate the effect of distributed surface roughness along the swept leading edges, with each one having a different level of roughness. As can be seen in Fig. 4, the straight nose section (labeled as LE-A) and one of the four swept leading edges (LE-B) were left pristine, with no laser ablation technique being applied to create roughness on the surface. The other three swept leading edges, labeled as LE-C, LE-D, and LE-E, had laser etching applied to create varying degrees of surface roughness on the PEEK model. This model was intended to be used to begin exploring the impact of surface roughness along swept leading edges of slender configurations. A first order issue was to investigate any impact due to phosphor coatings, thus LE-C was a replication of the roughness of a phosphor-coated ceramic model. Samples of phosphor coatings were used to model the surface in preparation for the etching process. Then, the remaining two swept leading edge locations, LE-D and LE-E, were intended to be two or three times rougher than the phosphors, respectively. Figure 4(b) shows that the small patches of distributed roughness do appear to be progressively rougher, although, in the process of etching, a small cavity was created at the boundary to the roughness patch. This was not intended, and for this reason the results obtained with this model are viewed as qualitative only. No attempt has been made to quantify the roughness, as new models without a cavity at the boundary of

the roughness patch are being pursued. The scans shown in Fig. 4(b) were obtained with a digital microscope with low magnification so as to allow imaging of the entire roughness patch, which was on the order of 19-mm (0.75-in) long.

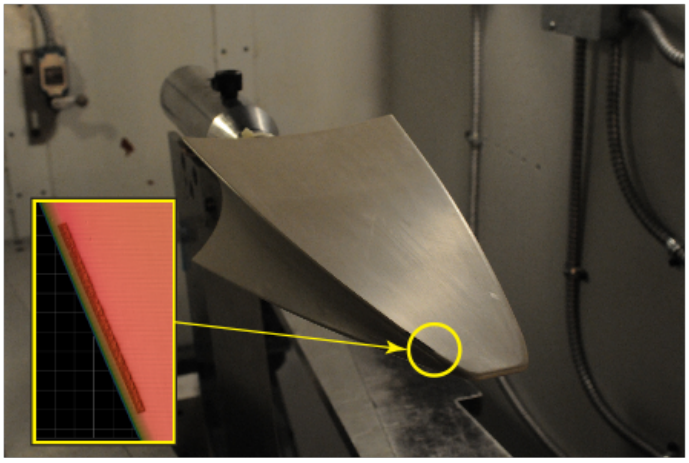
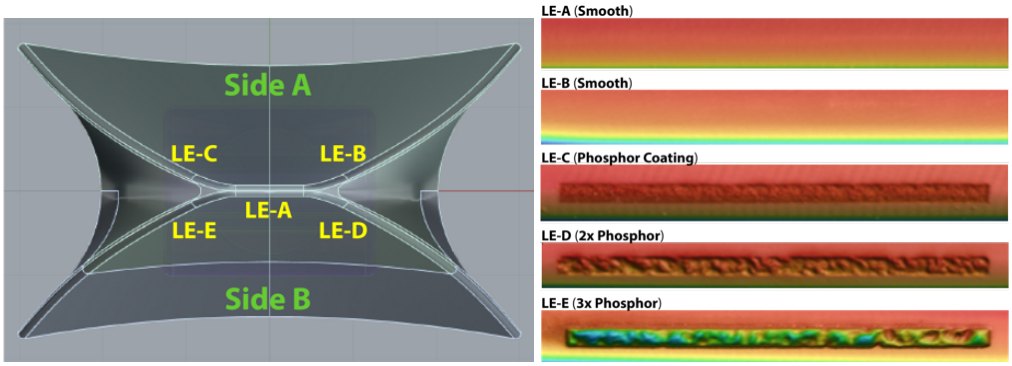


Fig. 3 One-third-scale BOLT PEEK model for the leading edge roughness test shown in the 20-Inch Mach 6 Air Tunnel in the retracted position. The inset provides a closeup of a leading edge with roughness laser etched onto surface.



(a) Front view of BOLT showing locations of roughness.

(b) Digital microscope images of five locations with varying degress of distributed roughness.

Fig. 4 PEEK model leading edge roughness details.

The model for the third test included the BOLT geometry, the aerodynamic fairings, and the TSM portion of downstream stack in order to investigate heating on the fairings and the TSM. The model was slip-cast ceramic for use with the phosphor thermography technique. On the flight vehicle, the TSM is 561-mm (22.1-in) long, and the aerodynamic fairings are 246-mm (9.7-in) long. The wind tunnel model was a quarter-scale model with a 216-mm (8.52-in) long BOLT geometry, a 140-mm (5.52-in) long TSM, and 61.5-mm (2.42-in) long fairings. The total model length was 356-mm (14.03-in) long. The model coordinate system and reference dimensions used for the TSM heating analysis are shown in Fig. 5. Figure 6 shows the model coated with phosphors, and installed in the retracted position of

the 20-Inch Mach 6 Air Tunnel.

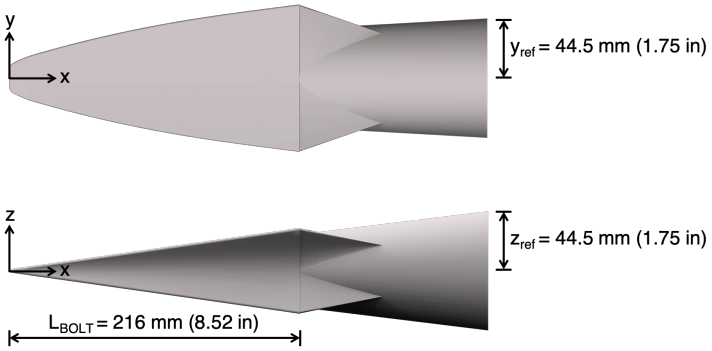


Fig. 5 Model coordinate system and reference dimensions for the TSM heating analysis of the quarter-scale model.

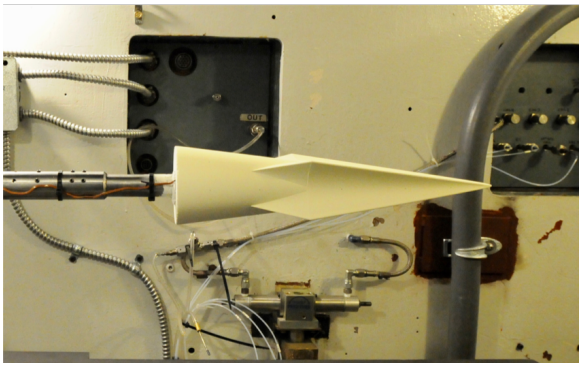


Fig. 6 Quarter-scale BOLT ceramic model for the TSM heating test shown in the 20-Inch Mach 6 Air Tunnel in the retracted position.

C. Test Conditions

As discussed in Ref. [3], the Re_L expected in flight for BOLT during the test window of interest varies from 1×10^6 to 20×10^6. The reference length is based on the length of the BOLT geometry; for the half-scale model, the Re_L range is 1.5×10^6 to 11.3×10^6, for the one-third-scale model, the Re_L range is 1.4×10^6 to 7.9×10^6, and for the quarter-scale model, the Re_L range is 1.4×10^6 to 5.6×10^6. The flight vehicle will be uncontrolled, but spin-stabilized at approximately 3.0 Hz, relying upon the vehicle's static margin to maintain aerodynamic stability. Assuming a successful exoatmospheric reorientation maneuver, BOLT should reenter at a nominal total angle of attack near zero degrees. However, combined angle of attack and sideslip excursions are likely, with less than ±2° being the desired goal but ±5° being acceptable. The wind tunnel test matrices for each test were set up to explore the impact of these excursions, in both pitch and yaw, on measured boundary layer transition results in order to understand the possible aeroheating environments on the model. The nominal reentry case refers to an $\alpha = 0°$ and $\beta = 0°$ model attitude.

In addition to varying the model attitude, the freestream Reynolds number was changed. Freestream conditions for

the Re_∞ values run during each test are listed in Tables 1- 3. The conditions are averaged values based on all runs at a given condition. For the two phosphor thermography tests, the models were run at two different viewing orientations in order to get heating data on both the top and side surface of the model.

Table 1 Tunnel Conditions for the Preliminary Transition Assessment Test.

Re_∞ (1/m)	Re_∞ (1/ft)	Re_L	M_∞	T_∞ (K)	ρ_∞ (kg/m^3)	U_∞ (m/s)
3.43×10^6	1.05×10^6	1.48×10^6	5.89	62.2	1.64×10^{-2}	930.6
6.64×10^6	2.02×10^6	2.87×10^6	5.96	62.9	3.16×10^{-2}	947.3
13.2×10^6	4.01×10^6	5.69×10^6	6.01	60.2	6.20×10^{-2}	948.0
26.2×10^6	7.98×10^6	11.3×10^6	6.03	60.0	1.21×10^{-1}	931.4

Table 2 Tunnel Conditions for the Leading Edge Roughness Test.

Re_∞ (1/m)	Re_∞ (1/ft)	Re_L	M_∞	T_∞ (K)	ρ_∞ (kg/m^3)	U_∞ (m/s)
4.49×10^6	1.37×10^6	1.37×10^6	5.92	62.3	2.14×10^{-2}	936.7
9.45×10^6	2.88×10^6	2.88×10^6	5.99	62.7	4.48×10^{-2}	949.7
17.6×10^6	5.35×10^6	5.35×10^6	6.03	63.8	8.35×10^{-2}	963.1
26.0×10^6	7.94×10^6	7.94×10^6	6.03	60.2	1.20×10^{-1}	933.5

Table 3 Tunnel Conditions for the Transition Support Module Heating Test.

Re_∞ (1/m)	Re_∞ (1/ft)	Re_L	M_∞	T_∞ (K)	ρ_∞ (kg/m^3)	U_∞ (m/s)
6.69×10^6	2.04×10^6	1.45×10^6	5.96	62.9	3.18×10^{-2}	947.2
13.2×10^6	4.03×10^6	2.86×10^6	6.01	62.2	6.23×10^{-2}	948.0
26.1×10^6	7.95×10^6	5.65×10^6	6.03	60.1	1.21×10^{-1}	932.2

D. Phosphor Thermography Technique

1. Data Acquisition and Reduction

Aeroheating data were obtained using two-color, relative-intensity, global phosphor thermography and reduced using the Imaging for Hypersonic Experimental Aeroheating Testing (IHEAT) software. The global phosphor thermography method uses slip-cast ceramic wind tunnel models coated with a thermographic phosphor compound. The models are illuminated by an ultraviolet light source, producing a temperature-dependent fluorescence of the phosphor coating. A three-color charge-coupled device (CCD) camera is used to take images of the model fluorescence intensity before a wind tunnel run in the wind-off condition and during a wind tunnel run when the model is exposed to hypersonic flow. Details of the phosphor thermography technique are provided in Refs. [9, 10].

The IHEAT software uses a phosphor calibration to convert the intensity data from each image pixel to a temperature. Convective heat transfer coefficients are then determined from the temperature time history using one-dimensional heat conduction theory assuming a step function in heat transfer beginning at the injection of the model into the tunnel. Heat transfer data from IHEAT are typically reported in terms of h/h_{FR}, where h_{FR} is the heat transfer film coefficient resulting from a Fay-Riddell computation for a reference hemisphere of a specified radius (in this case, the BOLT leading edge radius). Convective heat transfer coefficients are calculated from a convective heat transfer equation defined in terms of enthalpy as seen in Eq. 1:

$$h = q/(H_{AW} - H_W) = q/(H_0 - H_{300K}) \tag{1}$$

Details of the IHEAT software, including additional heat transfer calculation assumptions and equations are described in Refs. [9, 11].

2. Data Uncertainty

The error analysis presented in Ref. [9] provides an estimation of uncertainty for the phosphor thermography method. This error analysis includes error associated with the phosphor calibration, data acquisition, and data reduction to pixel-by-pixel heat transfer values in IHEAT. Additional uncertainty is due to tunnel flow quality, test-condition repeatability, and the two-dimensional mapping of image pixel location to the physical location on the model. The experimental uncertainty for convective heat transfer measurements based on the error analysis in Ref. [9] is typically between 8 and 10%. The uncertainty is dependent on the rise in model surface temperature, resulting in higher uncertainty and more scatter in the results when the model surface temperature rise is low. For the present case, with low windward heating, typical of slender vehicles (e.g., BOLT) with low-angle compression (or even flow expansions), significantly higher uncertainties are expected and are demonstrated by a higher amount of noise in the heating results.

With the exception of the lowest Re_L data (at approximately $Re_L = 1.4 \times 10^6$), based on the plot of estimated uncertainty vs. model surface temperature given in Ref. [9], the experimental uncertainty is on the order of 15% on the BOLT surface where the flow has transitioned to turbulent. The uncertainty ranges from 20% to 60% along the BOLT surface centerline where the flow appears to be resistant to transition and the surface temperature rise is low, on the order of 5-20 K. For the quarter-scale model that includes the TSM, the uncertainty on the TSM is approximately 20% where the surface temperature rise is on the order of 20 K.

In the plot of estimated uncertainty vs. model surface temperature given in Ref. [9], the curves are nearly asymptotic, tending toward infinity, for the temperature range for the lowest Re_L data (at approximately $Re_L = 1.4 \times 10^6$) and thus cannot be used as a basis for uncertainty estimates for these cases. However, as will be shown, test-to-test comparison of phosphor data at the lowest Re_L shows good repeatability despite the extremely low model surface temperature rise and

high data scatter. Additionally, the lowest Re_L data were in close agreement with predicted heating distributions using computational methods.

E. Infrared Thermography Technique

The phosphor thermography technique is LaRC's standard for aeroheating studies. However, the technique is not suitable for studies with vehicle configurations that require small and precise surface features, since the casting process and the phosphor surface coating can lead to decreased fidelity of the surface features. The phosphor coating is on the order of 0.001-in thick, so if the purpose of the study is to look at the effect of a feature that is on the same order, then significant discrepancies might be included in the observations. A newer test technique is under development at LaRC, whereby an IR camera is used to monitor the surface temperatures on very accurately milled models. The advantage of this approach is that surface deviations are not introduced due to the casting process (i.e., model shrinkage and/or micro-fractures), and an overcoat may not be required. For this study, the models were built from a relatively cheap resin material called PEEK (poly-ether-ether-ketone). The use of PEEK with IR has been reported in the literature for a few years (for instance, see Ref. [12]); thus, LaRC has taken steps recently to explore this material for use in aeroheating studies for cases which require stricter control of model fidelity. Although the PEEK models provided useful data for this study, with other model geometries, the PEEK material could reach maximum temperatures in the Langley Aerothermodynamics Laboratory facilities that would damage the models. Thus, other materials are currently being explored at LaRC to implement in the IR thermography technique for the hypersonic facilities. The IR setup for the present study consisted of a FLIR SC6701 SLS long-wave (7.5-9.5 μm) IR camera looking through a large zinc selenide window at the top of the tunnel. The camera, which provides 640x512 pixel resolution, comes with 25, 50, and 100 mm lens options. The camera framing rate was 60 Hz, and the camera lens, location, and view angle were set to optimize the size of model in the imager, while being as close to perpendicular as possible to the model surface of interest.

For the IR thermography technique using PEEK as a model substrate, heat transfer calculations presented herein were completed with an exploratory code called QQHeat, which applies the same heat transfer assumptions as IHEAT. QQHeat was developed previously, in support of the Shuttle program (see Ref. [13]), specifically for use with IR data. QQHeat was used to process this set of data since the existing IHEAT package has not been modified yet to work with the IR output files. Due to uncertainties associated with using PEEK in the IR technique at LaRC, for the present paper, the IR thermography results are included as qualitative data only to provide a parametric look at the transition patterns on the BOLT geometry for various wind tunnel conditions and vehicle positions. No uncertainty assessment is provided for the qualitative IR results.

F. Computational Method

The numerical results presented in this paper were computed using The Langley Aerothermodynamic Upwind Relaxation Algorithm (LAURA) [14, 15]. LAURA is a finite-volume shock-capturing structured-grid computational fluid dynamics (CFD) tool specialized for hypersonic reentry flows. Either the Euler, thin-layer Navier-Stokes, or full Navier-Stokes equations are relaxed in pseudotime to a steady state. First-order inviscid fluxes are constructed using Roe's flux difference splitting with Harten's entropy fix and are extended to second-order using Yee's Symmetric Total Variational Diminishing (STVD) limiting. Second-order central differences approximate the viscous fluxes. LAURA can utilize point or line-implicit relaxation and employs MPI to run efficiently on parallel computing architectures.

Solutions were computed for an angle of attack and a sideslip of zero degrees, therefore a quarter-body geometry was appropriate given the vehicle symmetry. Each grid was solution adapted for bow shock alignment and boundary layer clustering using the shock adaption algorithm in LAURA; this effectively distributes off-body points to provide credible heat transfer. Along each line normal to the surface, this algorithm redistributes points such that a limited number (i.e. 5) remain in the freestream and the cell height spacing at the wall is based on a user-prescribed wall cell Reynolds number (0.50). Having a machine zero L_2 error norm of the governing equation residuals or a percentage change in heating of less than 0.1% over 5000 iterations defined convergence.

The first set of solutions were computed for the BOLT geometry for comparison with the preliminary transition assessment wind tunnel test. Solutions were computed with laminar full Navier-Stokes on a computational mesh containing approximately 5.3 million cells (medium mesh) covering a quarter of the BOLT geometry. Figure 7 compares centerline heating results of a basic grid refinement study using three grid levels, with coarser grids constructed by removing every other surface point. The finest mesh consisted of 104 blocks with 33 x 33 x 201 points per block. The 201 points through the layer remained unchanged for all levels of mesh refinement. The left axis in Fig. 7 indicates the nondimensional heating levels, h/h_{FR}. Three computed heating results are shown for each level of refinement (coarse, medium, and fine), along with the heating value based on Richardson's Extrapolation. Richardson's method provides a representation of a spatially converged ($h \rightarrow 0.0$) solution and in this work Richardson's distribution is based on fine and medium mesh data. Note, if flow physics are not accurately captured, there is no guarantee a spatially resolved mesh will provide accurate values.

The grid convergence index (GCI [16]) as defined by Roache (Eq. 2), provides a conservative estimate of discretization error expressed as a percentage difference between a solution and it's asymptotic value at $h = 0$. The subscripts 1 and 2 represent the fine and medium levels, respectively, r is the spacing ratio, p is the order of the scheme, and f is the quantity of interest. The following constants were used for this work: r and p were two (2) and the factor of safety (Fs) was 3.0.

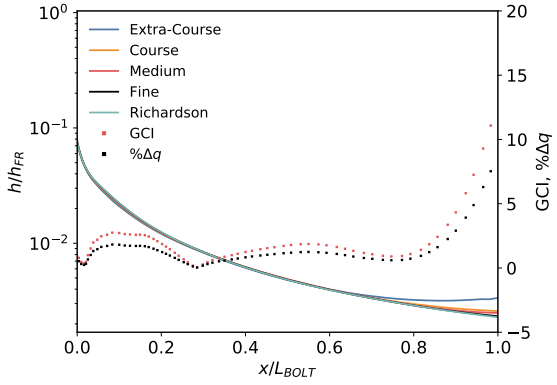


Fig. 7 Nondimensional heating and grid convergence index along the BOLT geometry model centerline for the nominal vehicle reentry attitude ($\alpha = 0°$, $\beta = 0°$).

$$GCI = 100.0 \cdot Fs \cdot \frac{\left|\frac{f_2 - f_3}{f_2}\right|}{(r^p - 1)} \tag{2}$$

The right axis of Fig. 7 presents the GCI based on surface heat rate. The GCI varies from nearly zero along the first half of the vehicle and increases to 13% over the latter half. The heating sensitivity to mesh refinement over the latter half is believed to be due to boundary layer build-up on the centerline. While 13% is not an insignificant percentage, the absolute change in heating towards the end of centerline is quite small. Also shown in right axis of Fig. 7 is the percent difference in surface heating for the medium grid and Richardson values. The conservative nature of the GCI is evident.

For comparison with the TSM heating test data, a second set of solutions were computed to include the BOLT geometry, aerodynamic fairings, and TSM. Figure 8 shows results of a four-level mesh refinement study, with coarser grids constructed by removing every other surface point. Plotted is nondimensional heating (h/h_{FR}) along the vehicle centerline for each grid level, with the finest grid consisting of 744 blocks with 33 x 33 x 129 points in each block (98 million cells). The 129 points through the layer remained unchanged for all levels of mesh refinement. While the BOLT centerline appears grid-converged, changes in mesh resolution continue, to a small degree, to influence TSM heating. Percent changes in heating between the medium grid and Richardson values were less than 1% on the BOLT Fight Geometry and 10% on the TSM. The highest percent differences occur where the heating is lowest, so the absolute change in heating is quite small. The medium mesh results were used for experimental data comparison. Like in Fig. 7, the right axis of Fig. 8 shows the GCI and percent difference in surface heating. The conservative nature of the GCI is once again shown.

Presented in the paper for the TSM heating comparison are laminar and turbulent (Cebeci-Smith, [17]) full Navier-Stokes solutions computed using a computational mesh containing approximately 25 million cells covering a quarter of the vehicle, including the TSM.

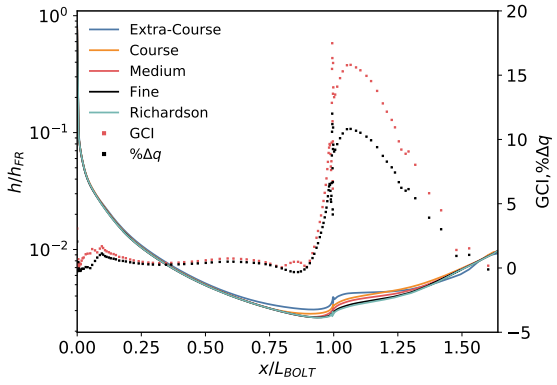


Fig. 8 Mesh refinement along model centerline for $Re_L = 1.4 \times 10^6$ at the nominal vehicle reentry attitude ($\alpha = 0°, \beta = 0°$).

IV. Results and Analysis

Multiple test entries into the NASA Langley 20-Inch Mach 6 Air Tunnel in support of BOLT will be discussed in the following subsections. First the boundary layer transition phosphor thermography results that were obtained prior to project kick-off are provided, with discussion of trends and observations. Then, the leading edge roughness test results obtained using IR thermography are presented. Finally, phosphor thermography results obtained to evaluate the aeroheating environment on the aerodynamic fairings and the Transition Support Module downstream of the BOLT experiment are provided.

A. Preliminary Transition Assessment

The initial test was a preliminary transition assessment on the BOLT geometry. Global surface convective heating data were obtained from 43 runs for a range of angle of attack, sideslip, Reynolds number, and model views using phosphor thermography on a half-scale ceramic model. Figure 9 provides global heat transfer images for a range of model length Reynolds numbers (Re_L) for BOLT at a nominal angle of attack ($\alpha = 0°$) and sideslip ($\beta = 0°$). This Re_L sweep is sufficient to reveal the systematic movement of transition, indicated by boundary layer transition onset fronts seen as two higher-heating lobes, symmetric on either side of the model centerline. At the lowest Re_L, Fig. 9a, the lobes are just appearing near the back end of the model, while at the highest Re_L, Fig. 9d, the lobes have moved forward to be closer to the nose and nearly extend outward to the swept leading edges. The central region (along the model centerline) appears resistant to transition, while the outboard sections (nearer to the swept leading edge) are much more sensitive to increasing Reynolds number. As reported in Ref. [18] from observations gleaned from supporting CFD, the central region is characterized by a thick boundary layer due in part to inflow coming from the swept leading edge. This central region does not appear "well-modeled by most instability codes" [18] and therefore, is considered a challenging region for the BOLT team to understand. The outer regions, on the other hand, are more traditional, with a thinner boundary layer. Instability calculations suggest that both second mode and crossflow instabilities are amplified in this outer region.

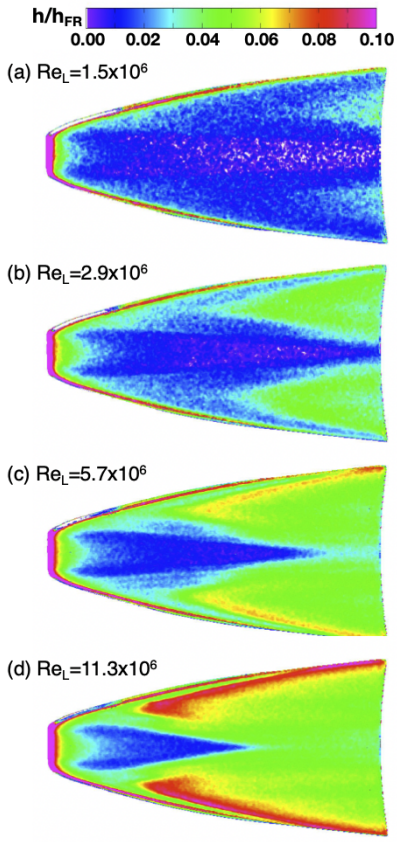


Fig. 9 Effect of Reynolds number at the nominal vehicle reentry attitude ($\alpha = 0°, \beta = 0°$).

Reference [18] also includes experimental IR and temperature sensitive paint (TSP) results from Purdue University's Mach 6 Quiet Tunnel, showing boundary layer transition patterns for both noisy and quiet flow. In the quiet results, only vortices are observed as boundary layer transition onset does not occur even at the highest Re condition available. However, for the noisy results, boundary layer transition onset fronts are seen that are similar to what is shown here (two lobes on either side of the centerline). Since the outboard regions are Reynolds number sensitive, it is quite likely that instability mechanisms are contributing to the observed results. There are even hints of streaks just ahead of the transition fronts, which provides further connectivity to the quiet tunnel results and the instability calculations of Ref. [18].

Figure 10 provides a comparison of extracted centerline heating data from the range of Re_L at a nominal angle of attack and sideslip to CFD predictions. Only the $Re_L = 2.9 \times 10^6$ case is shown for CFD as the laminar CFD results do not vary significantly with Reynolds number. This is a fairly typical comparison of the phosphor results to CFD, showing that the test technique compares favorably against predictions. As noted in the data uncertainty discussion, due to the low heating condition the phosphor scatter is quite high especially at the lower Reynolds numbers.

Figure 11 provides the global heat transfer images for a range of angles of attack from $\alpha = \pm 5°$ for fixed

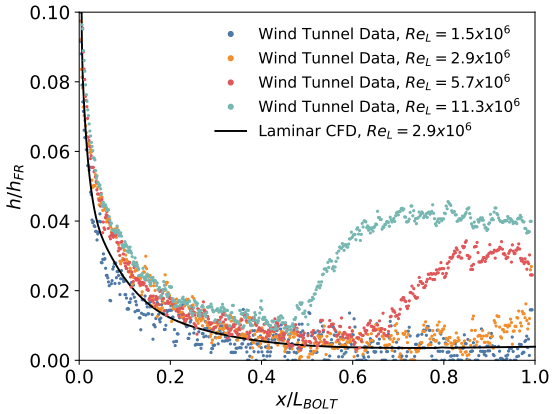


Fig. 10 Comparison of heating data and CFD at the nominal reentry attitude ($\alpha = 0°$, $\beta = 0°$).

$Re_L = 5.7 \times 10^6$ and $\beta = 0°$. From a trend perspective, increasing α for a fixed Re_L results in the symmetric boundary layer transition lobes on the windward side progressing slowly toward the nose. However, the relative impact of α appears somewhat less than the influence of Re_L. For instance, the transition front at $\alpha = 5°$, Fig. 11e, is not nearly as far forward as the highest Re_L at $\alpha = 0°$, Fig. 9d. A doubling of Re_L (compare Figs. 9c to 9d) has more influence on the transition fronts than an increase in angle of attack of two-and-a-half times (compare against Figs. 11d and 11e). For negative angles of attack (resulting in the measurement surface being on the leeside), the transition front appears largely stationary. Although, for the case of $\alpha = -5°$ (Fig. 11a), pronounced streaks emanate from the outboard region of the 2D nose section, perhaps an indication of a different boundary layer transition mechanism becoming important. As noted in Ref. [18], α effects for BOLT do not strongly affect the patterns much under quiet conditions: "The results are quite similar at each angle, though the number of crossflow streaks and the specific path vary slightly."

Figure 12 provides the global heat transfer images for a range of sideslip angles from $\beta = 0°$ to $5°$ for $\alpha = 0°$ and $Re_L = 5.7 \times 10^6$. Due to symmetry, only results from sideslip in one direction are shown. In comparison to the nominal $\beta = 0°$ case, there is no significant change in the relative sizes of the two lobes for $\beta = 2°$ (Fig. 12b). But for $\beta = 5°$ (Fig. 12c), the resulting boundary layer transition onset fronts are very asymmetric, with the side toward the flow becoming slightly larger and the side away becoming significantly smaller. In reference to the central (low heating) region, 2° sideslip resulted in a shift away from the centerline of less than a quarter of the span, while the shift was almost half the span away from the centerline for 5° sideslip. Reference [18] notes: "It is clearly evident that the BOLT geometry is much more sensitive to sideslip than angle of attack. The streak paths are shifted dramatically at 4-deg β." Understanding this sensitivity will become especially important for design of the instrumentation layout for the flight vehicle.

Sample combinations of off-nominal α and β on the global heat transfer results are provided in Figure 13. While other combinations were obtained, only a few of the most interesting cases are included here. As one might expect,

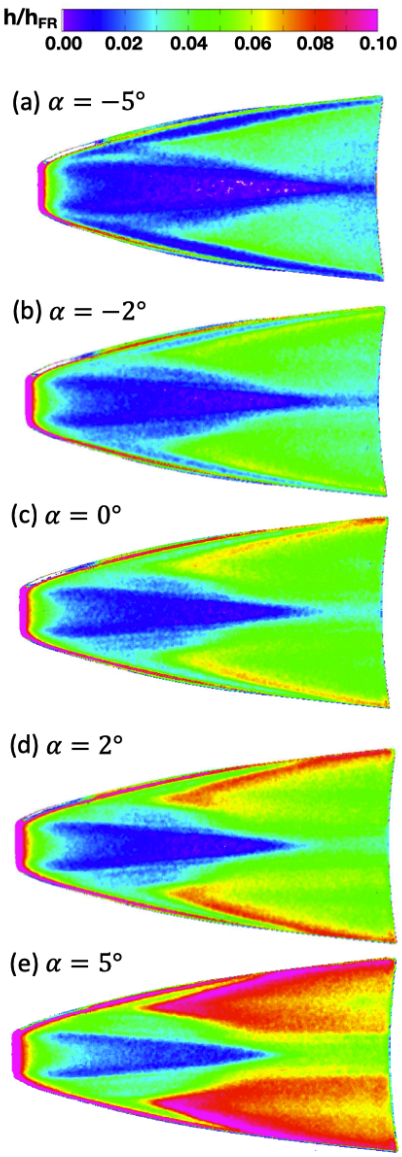


Fig. 11 Effect of angle of attack for nominal $\beta = 0^\circ$ and $Re_L = 5.7 \times 10^6$.

extreme combinations of α and β result in very asymmetric heating patterns (see Fig. 13c). Unfortunately, for a spin-stabilized sounding rocket, the actual α and β at the time of interest with post-flight data analysis will not be known a priori. These extreme cases with combined α and β effects are intended to provide guidance for determining whether any post-flight wind tunnel entries might be required for comparison against the flight data.

Figure 14 provides the global heat transfer images for the BOLT gutter region for a range of Re_L at nominal α and β. Results in the gutter were obtained for other α and β (and combinations), which were presented to the BOLT project at the kickoff, but these data are not included here. This was the first test entry conducted for the BOLT project that

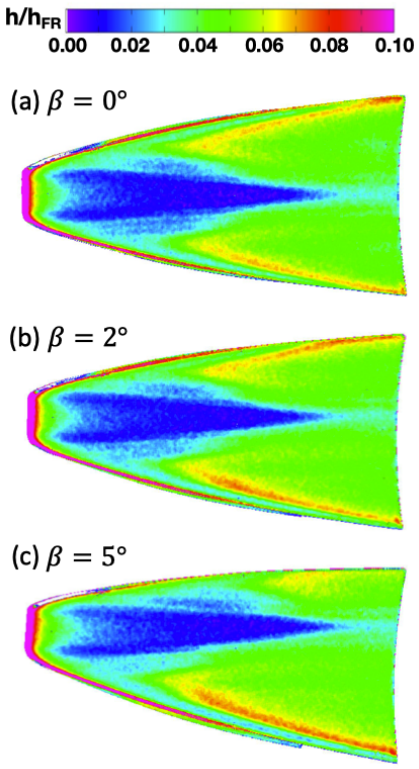


Fig. 12 Effect of sideslip for nominal $\alpha = 0^\circ$ and $Re_L = 5.7 \times 10^6$.

included data from the gutter region. It is interesting to note that the boundary layer transition patterns in the gutter at the highest Re_L look qualitatively similar to the results on the main surface (symmetric lobe fronts nearly 75% of the way up the forebody with a central laminar region) except that the image looks compressed. While the gutter region is not a focus for BOLT, the flight vehicle will be instrumented in the gutter region.

B. Leading Edge Roughness

To assess the influence of surface roughness on the transition front observations discussed previously, a separate study was initiated for which a one-third-scale model was built from PEEK and IR was used as the test technique. Global surface heating data were obtained from 98 runs for a range of angle of attack, sideslip, and Reynolds number. The intent of this study was to utilize both sides of the BOLT model to provide four swept leading edges with different levels of surface roughness with one left pristine (or smooth) and the other three having a laser ablation technique applied to create increasing levels of roughness (see Fig. 4). Thus, Side A of the model includes the smooth and phosphor-replicated leading edges, LE-B and LE-C, and Side B has leading edges LE-D and LE-E that are two and three times (notionally) rougher than the phosphor coating, respectively. Figure 15 provides the results of an angle of attack and Reynolds number sweep for Side A. In the montage captured in Fig. 15, the bottom half of each run image

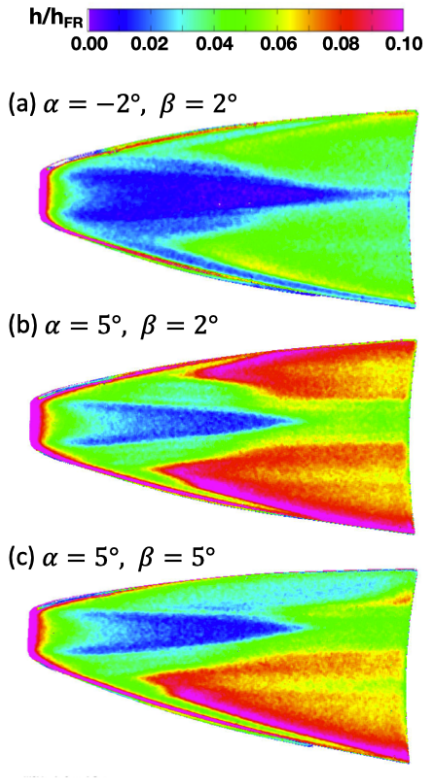


Fig. 13 Comparison of results for various angles of attack and sideslip at $Re_L = 5.7 \times 10^6$.

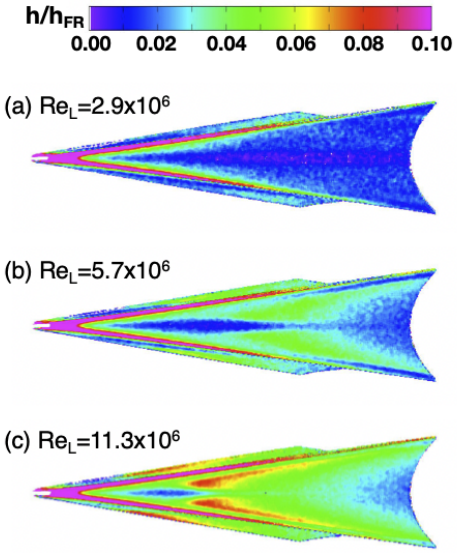


Fig. 14 Effect of Reynolds number on the side gutter at nominal $\alpha = 0°$ and $\beta = 0°$.

corresponds to the smooth LE and the top to the LE with the replicated phosphor coating. One can see by comparing top to the bottom of the image over this angle of attack and Re_L range that the resulting transition fronts look qualitatively

similar, which would suggest that the typical phosphor coatings are insufficient to significantly alter boundary layer behavior or transition fronts. The run images shown in this figure have been converted to heat transfer coefficients (consistent with the previous phosphor results), however, the heat transfer coefficient scale is not included here as these images are intended to only provide a relative assessment of the movement of the transition fronts.

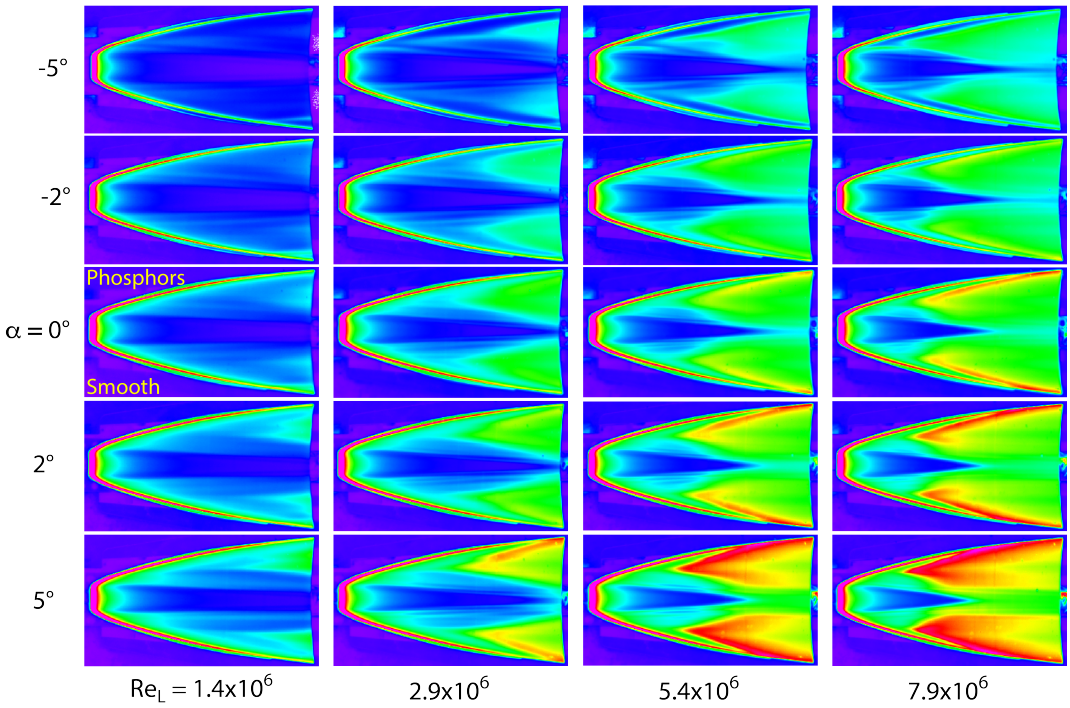


Fig. 15 Global heating results for Side A of the model for a range of angle of attack and Reynolds number. Side A of the model includes the smooth and phosphor-replicated leading edges, LE-B and LE-C.

Figure 16 provides the corresponding results of the angle of attack and Reynolds number sweep for Side B. By comparing these two figures, one can see that the rougher leading edges do in fact change the transition fronts. Small colored circles have been added to Fig. 16 as an indication of the authors' interpretation of the cases that show a significant (red) or somewhat less than significant (white) difference to the onset locations between corresponding cases shown in Figs. 15 and 16. A significant change was interpreted as when the entire boundary layer transition front was noticeably different, while the cases with a strong localized streak and not much movement of the front was considered a smaller change.

A secondary objective of the leading edge roughness study was to provide a comparison of heat transfer visualizations between the ceramic phosphor thermography technique and PEEK IR thermography technique. The IR images are less noisy than the phosphor results, especially in the lower heating central region, thus providing better clarity of streaks on the BOLT surface. In contrast to the phosphor thermography approach where only the model fluoresces and is therefore seen by the camera, the IR camera picks up a signal from everything in its view, including the injection plate below the model. Thus, the cropped IR images shown in Figs. 15 and 16 include the background, pending a method to strip out all

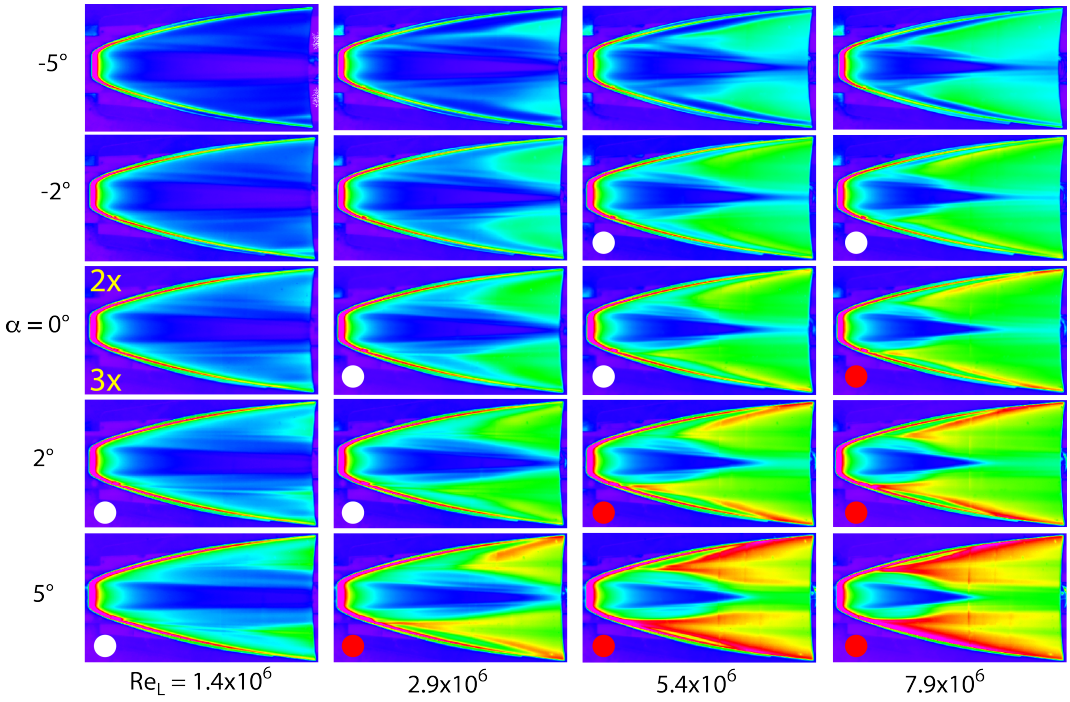


Fig. 16 Global heating results for Side B of the model for a range of angle of attack and Reynolds number. Side B of the model includes leading edges LE-D and LE-E that are two and three times rougher than the phosphor coating.

but the model. While further work is required with the IR thermography approach to advance it to quantitative status, two things stand out as positives attributes: (1) the lack of noise in the results, even for a case such as this, with low heating, and (2) the consistent results between test techniques for identifying transition onset.

C. Transition Support Module Heating

A third test was completed to investigate the aeroheating environments on the aerodynamic fairings and transition support module of the launch stack due to potential flow separation and reattachment from the BOLT Flight Geometry. Global surface convective heating data were obtained from 49 runs for a range of angle of attack, sideslip, Reynolds numbers, and model views using phosphor thermography on a quarter scale ceramic model. The results and analysis of data from this study focus on the fairings and the TSM region of the model. First, global surface heating for the nominal vehicle reentry case ($\alpha = 0°$, $\beta = 0°$) is shown along with a comparison of wind tunnel heating data and computational predictions along the model centerline and at an aft axial station. Then, global surface heating for two off-nominal vehicle reentry cases are shown along with a comparative analysis of heating on the TSM for the different vehicle reentry cases.

1. Nominal Surface Heating Data

Figure 17 provides global heating distributions for three Re_L conditions at the nominal vehicle reentry case. Consistent with previous results in the preliminary transition assessment study, there is a systematic movement of transition with increasing Re_L, evidenced by the development of two higher-heating lobes on either side of the model centerline. The focus of this test was on the fairings and the TSM region of the model. A complex flow field downstream of the BOLT Flight Geometry creates areas of localized heating on the TSM due to compression and shock boundary layer interactions. However, the peak heating values on the TSM are significantly lower than the peak heating values on the BOLT Flight Geometry. The fairings exhibit even lower heating than the TSM. Preliminary global heating distributions on the fairings and TSM were presented at the BOLT CDR four weeks after finalizing the model geometry.

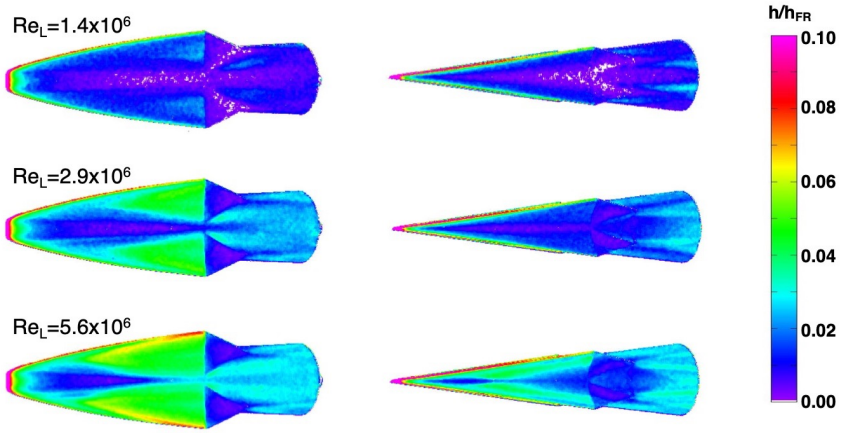
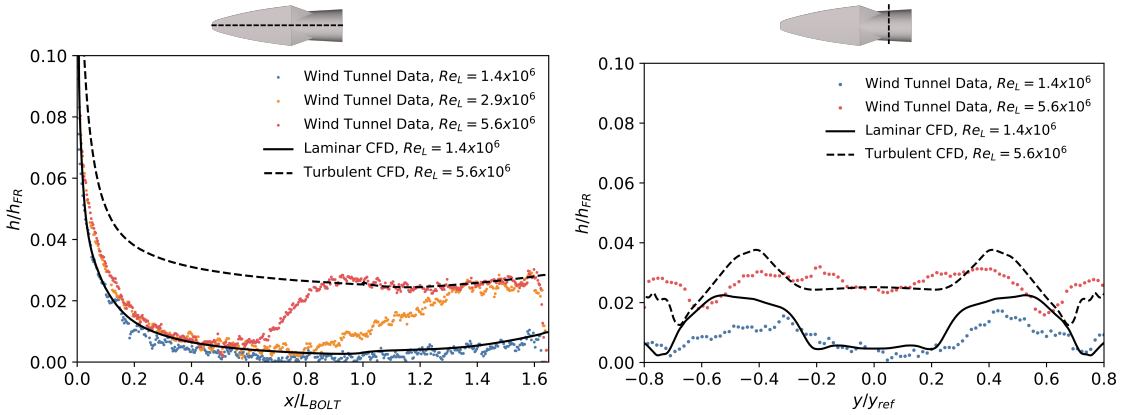


Fig. 17 Global heating distributions at the nominal vehicle reentry attitude ($\alpha = 0°, \beta = 0°$).

Figure 18 provides a comparison of extracted heating data from the wind tunnel nominal global heating distributions and the CFD predictions. Figure 18(a) compares fully laminar and fully turbulent CFD predictions to the model centerline heating for three Re_L cases. The laminar CFD solution for the $Re_L = 1.4 \times 10^6$ case compares well to the wind tunnel heating data for the same condition and shows a slight offset in the laminar regions of the higher Re_L cases. The turbulent CFD solution for the $Re_L = 5.6 \times 10^6$ case shows good agreement with the wind tunnel heating data for the same condition after transition occurs. Figure 18(b) compares heating along an axial station just aft of the fairings on the TSM. The wind tunnel data and CFD predictions match reasonably well, although less closely than along the model centerline. Both the wind tunnel data and the CFD predictions show higher heating streaks on either side of the centerline. The streaks are more pronounced and have higher peak heating in the CFD predictions. Given the low model surface temperature rise and the simple two-dimensional method used to extract linecuts within IHEAT, the axial TSM CFD predictions and wind tunnel data show reasonable agreement.

Figure 19 provides a test-to-test comparison of centerline heating on the BOLT geometry between the preliminary



(a) Model centerline data.

(b) Axial data at x/L_{BOLT}=1.32.

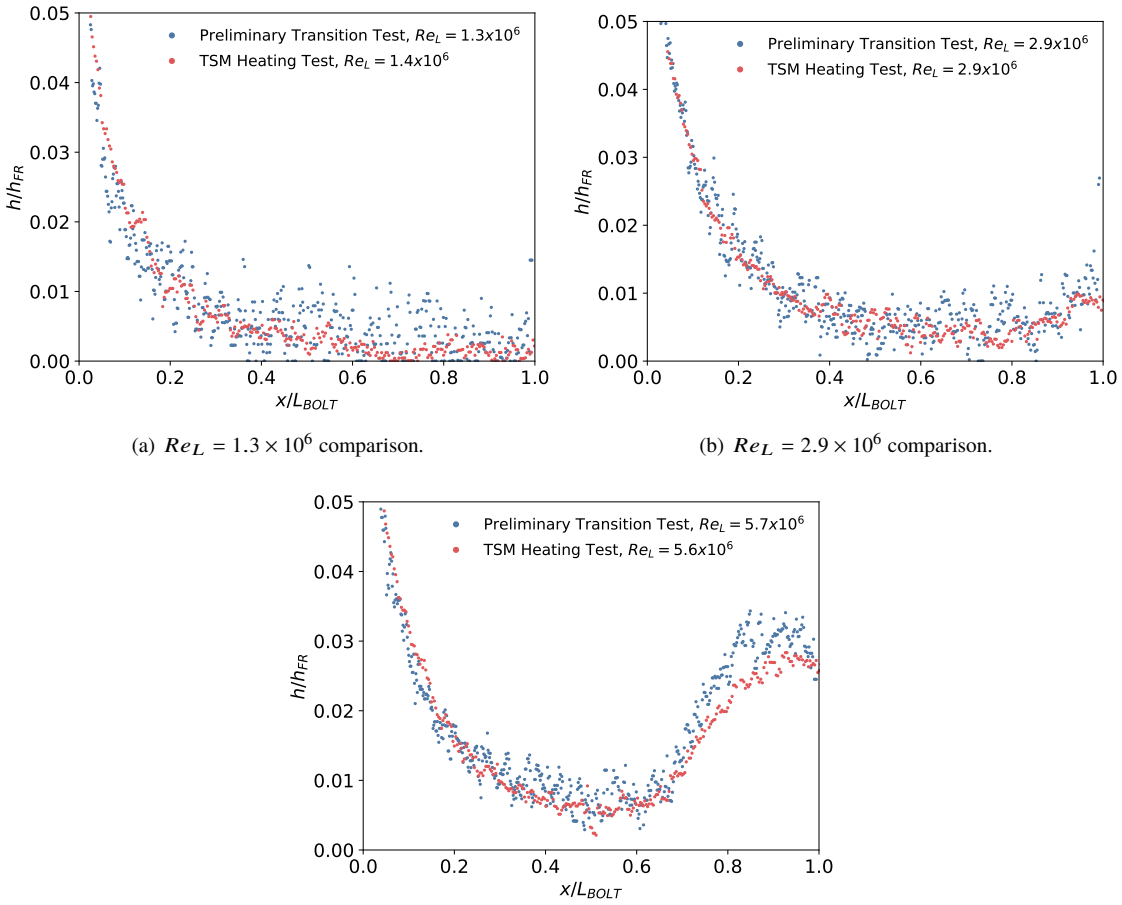
Fig. 18 Comparison of heating data and CFD at the nominal vehicle reentry attitude ($\alpha = 0°$, $\beta = 0°$).

transition assessment test and the TSM heating test. The preliminary transition assessment test was completed on a half scale BOLT model and the TSM heating test was completed on a quarter scale BOLT model with the TSM section and fairings. The data are compared by Re_L to account for the different model sizes. As discussed previously, the low heating along the BOLT centerline, especially at the lowest Re_L condition, leads to significant uncertainty and scatter in the data. However, the repeatability of the heating values between the two tests is acceptable given that these data are from different scale models with low surface temperature rise conditions. Overall, the CFD and the test-to-test comparisons provide confidence that the wind tunnel data are useful even with the higher uncertainty due to low model surface temperature rise on the TSM.

2. Off-Nominal Surface Heating Data

After the BOLT CDR, the BOLT team at JHU/APL completed a thermal analysis of the BOLT fairings and the TSM. The purpose of this thermal analysis was to determine expected temperatures on the fairings and the TSM and the potential need for thermal protection on these parts. The analysis was done for the nominal vehicle reentry angle of attack with several conservative assumptions, including a 1.2 factor of safety on the calculated heat transfer coefficient, which was in turn used to calculate the thermal response. The heating data from this test were used as a comparison point to see how the heating for an off-nominal total angle of attack excursion compared to heating for the nominal reentry angle of attack.

For the present analysis, two off-nominal cases were considered. The first was an $\alpha_T = 2°$ reentry case and the second was an $\alpha_T = 5°$ reentry case. The flight vehicle will be spin stabilized on reentry and therefore, will roll through various combinations of α and β for a set α_T. In order to capture an average value for heating on the TSM during a roll cycle, four model attitudes were used in the analysis. For the $\alpha_T = 2°$ reentry case, model attitudes of (1) $\alpha = 2°$, $\beta = 0°$, (2) $\alpha = 0°$, $\beta = 2°$, (3) $\alpha = 0°$, $\beta = -2°$, and (4) $\alpha = -2°$, $\beta = 0°$ were considered. Similarly, for the $\alpha_T = 5°$



(a) $Re_L = 1.3 \times 10^6$ comparison.

(b) $Re_L = 2.9 \times 10^6$ comparison.

(c) $Re_L = 5.7 \times 10^6$ comparison.

Fig. 19 Comparison of centerline heating data from the preliminary transition assessment test and the TSM test at the nominal vehicle reentry attitude ($\alpha = 0°, \beta = 0°$).

reentry case, model attitudes of (1) $\alpha = 5°, \beta = 0°$, (2) $\alpha = 0°, \beta = 5°$, (3) $\alpha = 0°, \beta = -5°$, and (4) $\alpha = -5°, \beta = 0°$ were considered.

Due to the symmetry of the BOLT geometry, the top surface $\pm\beta$ cases and the side surface $\pm\alpha$ cases are symmetric. To confirm that the wind tunnel heating data could be considered symmetric in these instances, a symmetry check was conducted for a $\beta = \pm 2°$ top surface view case. Figure 20 shows heating data extracted at an axial station at $x/L_{BOLT} = 1.32$ on the TSM for the $\alpha = 0°, \beta = 2°$ and $\alpha = 0°, \beta = -2°$ model attitudes. A symmetric reflection of the $\alpha = 0°, \beta = 2°$ data across the $y/y_{ref} = 0$ centerline shows good agreement with the $\alpha = 0°, \beta = -2°$ case. Symmetric reflection of the data was used for subsequent symmetric cases (e.g., the top surface $\alpha = 0°, \beta = -5°$ data are symmetric reflections of the top surface $\alpha = 0°, \beta = 5°$ data).

Global surface convective heating data for the $\alpha_T = 2°$ and $\alpha_T = 5°$ off-nominal reentry cases are shown in Figs. 21- 24. Figure 21 provides heating data for the $\alpha_T = 2°$ reentry case at $Re_L = 2.9 \times 10^6$. As expected, heating on the TSM is higher on the windward side of the vehicle compared to the leeward side of the vehicle. On the top surface,

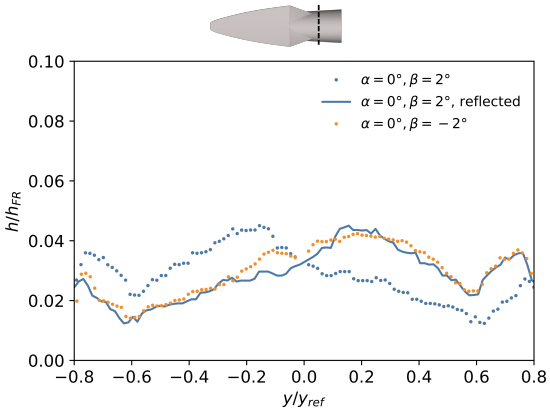


Fig. 20 Data symmetry confirmation for $\beta = \pm 2°$ at x/L$_{BOLT}$=1.32 for $Re_L = 5.6 \times 10^6$.

the $\beta = \pm 2°$ model attitudes show a change in heating pattern on the TSM as compared to the nominal case. In these sideslip attitudes, the asymmetric transition fronts on the BOLT Flight Geometry result in higher heating on one side of the TSM. On the side surface, heating asymmetry occurs with $\alpha = \pm 2°$ resulting in stronger heating streaks on the windward side of the top surface. In all cases, heating on the fairings was very low.

Similar heating trends discussed in the above paragraph exist for all four reentry cases considered in this analysis. TSM heating increases with Re_L and with model angle of attack. Heating on the fairings is low for all model attitudes with some heating starting to develop in the $\alpha = -5°$, $\beta = 0°$ attitude on the forward portion of the fairing that is attached to the BOLT Flight Geometry. In all cases, peak heating on the TSM is lower than peak heating on the BOLT top surface.

To compare heating for an off-nominal total angle of attack excursion with heating for the nominal reentry angle of attack, heating data were extracted along two axial stations on the TSM as indicated in Figure 25. Station A was just beyond the fairing tips at $x/L_{BOLT} = 1.32$ and station B was further downstream on the TSM at $x/L_{BOLT} = 1.48$. Heating values at each station across the four model attitudes were averaged to represent average heating over an $\alpha_T = 2°$ or $\alpha_T = 5°$ roll cycle. An example is shown in Fig. 26; heating along the station A cut on the top surface is plotted for the four model attitudes considered for an $\alpha_T = 5°$ roll cycle. The black line shows the resulting average of the four cuts.

The 2° and 5° averaged heating values for the top and side surfaces for $Re_L = 2.9 \times 10^6$ and $Re_L = 5.6 \times 10^6$ were plotted against the 0° heating at the corresponding axial station. Figure 27 provides heating comparisons for the $Re_L = 2.9 \times 10^6$ data and Fig. 28 provides heating comparisons for the $Re_L = 5.6 \times 10^6$ data. The off-nominal reentry averaged heating is generally higher than the 0° reentry heating. In order to quantitatively compare the off-nominal case to the nominal case, the maximum heating value for each case was used as this represents the peak heating to the TSM material. For example, using the data in Fig 28(a), the maximum heating value for the averaged 5°, top surface, $Re_L = 5.6 \times 10^6$ data was divided by the maximum heating for the 0°, top surface, $Re_L = 5.6 \times 10^6$ data to get

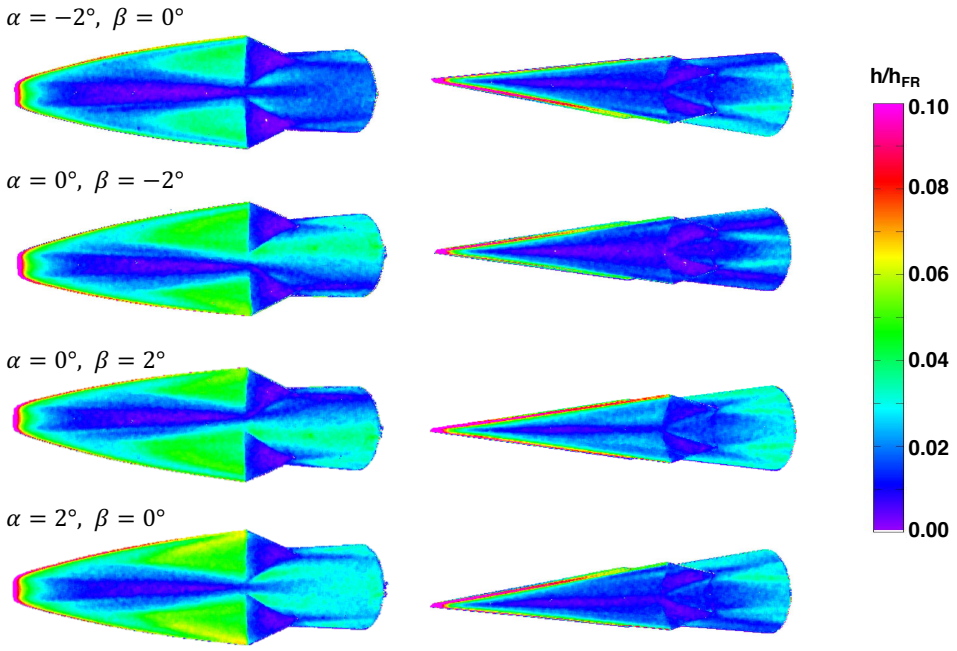


Fig. 21 Global heating distributions representing an $\alpha_T = 2°$ off-nominal vehicle reentry attitude for $Re_L = 2.9 \times 10^6$.

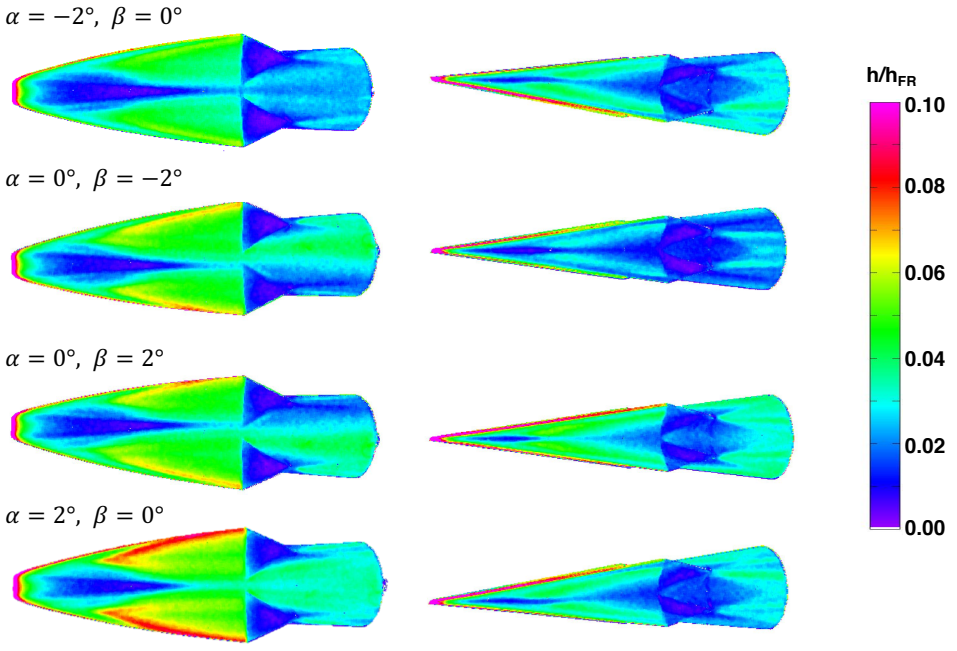


Fig. 22 Global heating distributions representing an $\alpha_T = 2°$ off-nominal vehicle reentry attitude for $Re_L = 5.6 \times 10^6$.

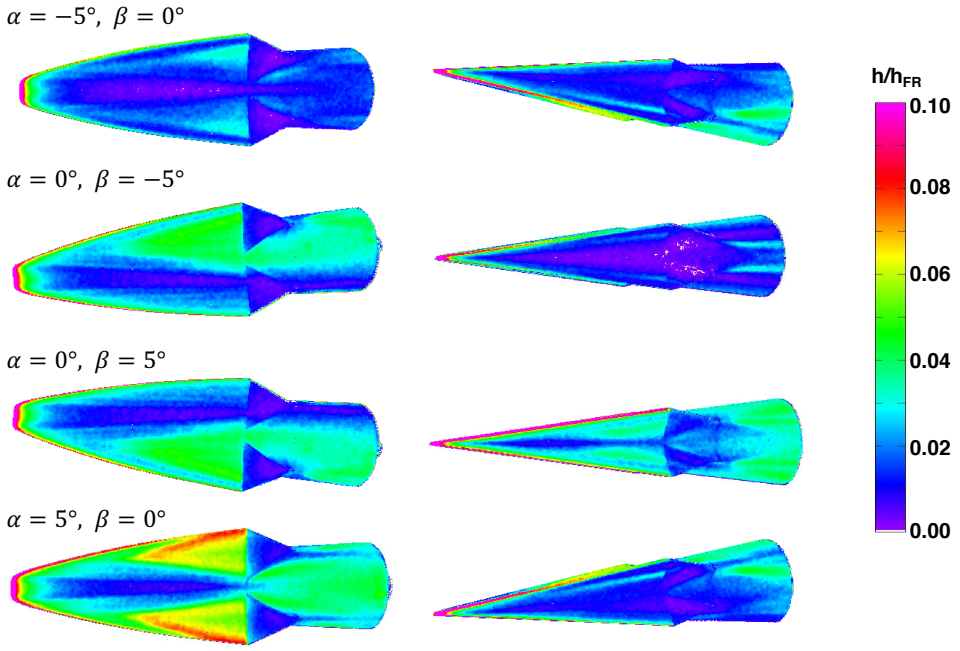


Fig. 23 Global heating distributions representing an $\alpha_T = 5°$ off-nominal vehicle reentry attitude for $Re_L = 2.9 \times 10^6$.

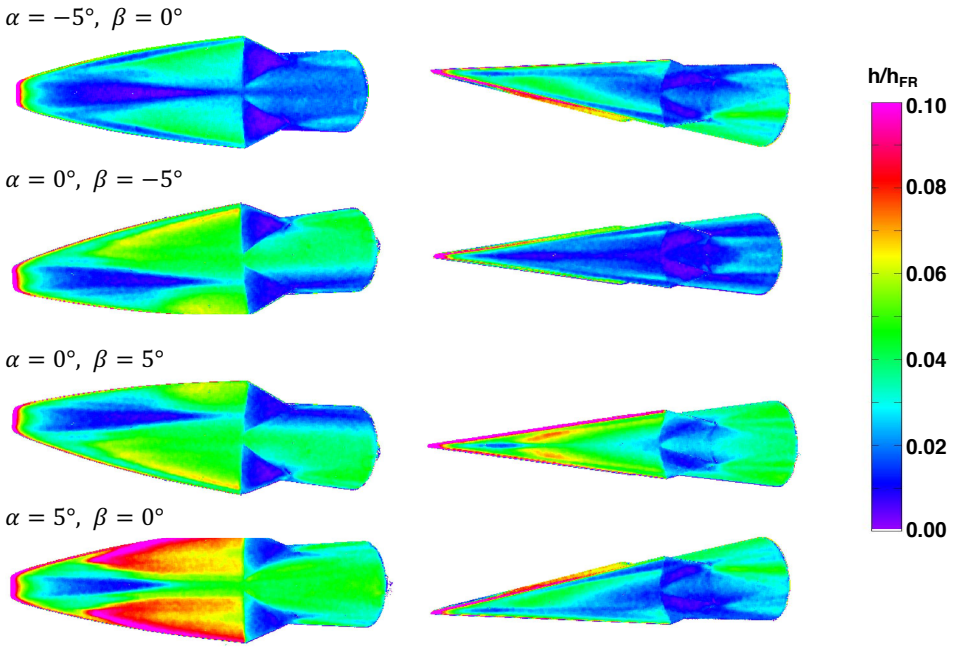


Fig. 24 Global heating distributions representing an $\alpha_T = 5°$ off-nominal vehicle reentry attitude for $Re_L = 5.6 \times 10^6$.

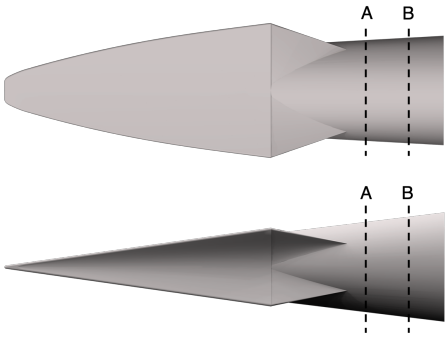


Fig. 25 TSM axial station locations.

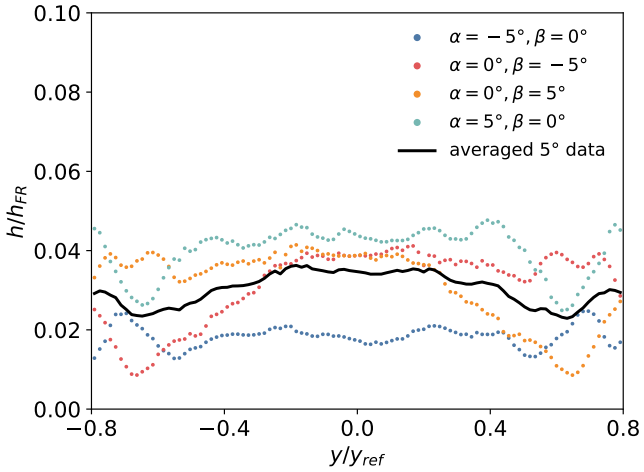


Fig. 26 Example average heating calculation on the top surface at station A for $Re_L = 5.6 \times 10^6$, representing an $\alpha_T = 5°$ vehicle reentry attitude.

a maximum heating ratio. This tabulation was done for each comparison case and the results are shown in Table 4.

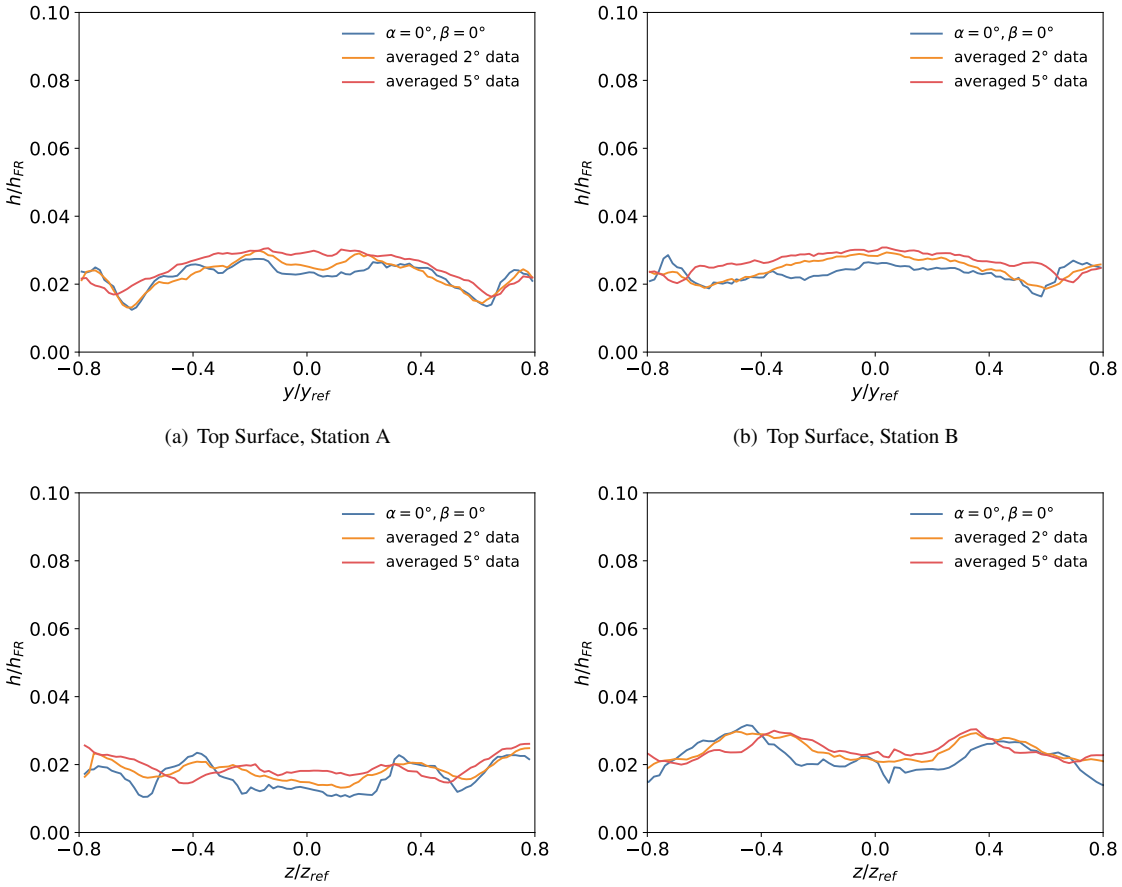
Table 4 Off-nominal to nominal reentry angle-of-attack heating ratios.

Angle	Surface	Re_L	Max Heat Ratio Station A	Max Heat Ratio Station B
2°	Top	2.9×10^6	1.09	1.03
2°	Side	2.9×10^6	1.06	0.94
5°	Top	2.9×10^6	1.12	1.08
5°	Side	2.9×10^6	1.11	0.96
2°	Top	5.6×10^6	1.08	1.13
2°	Side	5.6×10^6	1.03	0.93
5°	Top	5.6×10^6	1.15	1.19
5°	Side	5.6×10^6	1.08	0.96

The results in Table 4 show that for all cases considered in this analysis, the maximum heating value for the off-nominal reentry case is less than 20% higher than the maximum heating value for the nominal reentry case. The highest maximum heating ratio occurred for the 5°, top surface, $Re_L = 5.6 \times 10^6$ case. The lowest maximum heating ratios occurred on the side surfaces at station B. This wind tunnel data analysis supports the 1.2 factor of safety on the heat transfer coefficient used in the JHU/APL thermal analysis that was done for a nominal $\alpha_T = 0°$ reentry.

V. Summary

An overview of support by LaRC to the BOLT flight project has been discussed, including an early phosphor thermography wind tunnel study on a half-scale model, a leading edge roughness IR thermography study on a one-third-scale model, and an assessment of heating on the BOLT aerodynamic fairings and the TSM on a quarter-scale



(a) Top Surface, Station A

(b) Top Surface, Station B

(c) Side Surface, Station A

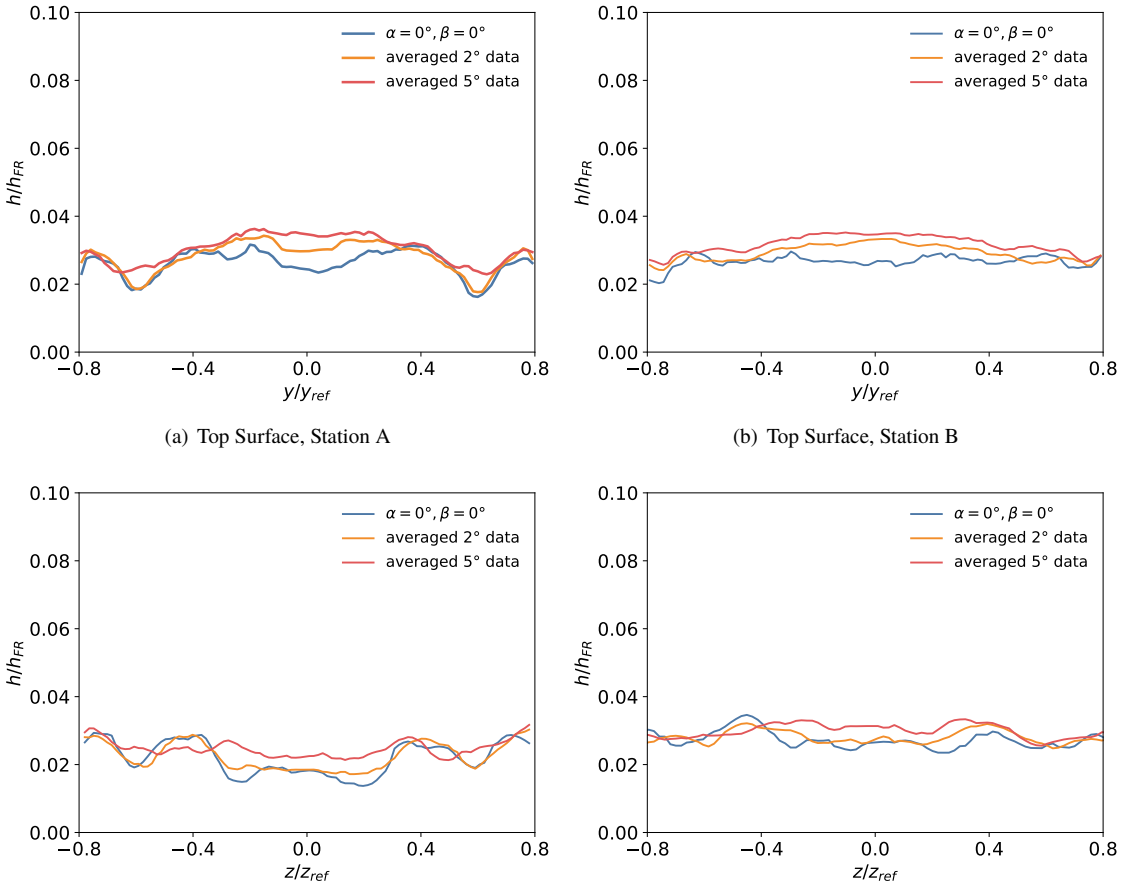
(d) Side Surface, Station B

Fig. 27 Off-nominal and nominal TSM heating comparison for $Re_L = 2.9 \times 10^6$.

model.

A preliminary transition assessment study using phosphor thermography was conducted to assemble a parametric database of transition behavior on the BOLT geometry. Results from this study were provided at the BOLT project kickoff meeting. This initial wind tunnel entry provided an understanding of the movement of the transition onset fronts with changing Reynolds number, angle of attack, and sideslip. The most significant trend was the observation of a two-lobed transition pattern, symmetric on either side of the centerline, that was strongly influenced by an increase in Reynolds number. This two-lobed pattern appeared rather insensitive to model angle of attack over the range of interest (±5°). Sideslip more strongly affected the symmetry of the patterns for the same range. Flight instrumentation was placed with consideration of this sideslip sensitivity.

An IR thermography study was conducted to consider the effects of leading edge roughness on the BOLT transition behavior. The four swept leading edges of the PEEK model varied in roughness from smooth to three times the roughness of the typical phosphor coating applied to ceramic models used in LaRC's phosphor thermography technique. The



(a) Top Surface, Station A

(b) Top Surface, Station B

(c) Side Surface, Station A

(d) Side Surface, Station B

Fig. 28 Off-nominal and nominal TSM heating comparison for $Re_L = 5.6 \times 10^6$.

qualitative heat transfer data derived from the IR temperature results for this study (over a range of Reynolds number and angle of attack) show that the typical phosphor coating roughness is insufficient to significantly alter boundary layer behavior or transition fronts. As the leading edge roughness was increased to two and three times the roughness of the typical phosphor coating, in some cases a significant difference in boundary layer transition onset location occurred. Typically, either the transition onset lobe on the side with the greater roughness moved farther forward toward the nose of the vehicle, or the increased roughness induced a localized heating streak that did not substantially change the onset lobe heating position.

Finally, an evaluation of the aeroheating environment on the BOLT aerodynamic fairings and the TSM was completed prior to the BOLT CDR. The global heating distributions showed low heating on the fairings and on the TSM as compared to the BOLT Flight Geometry surface. TSM heating increased with increasing Re_L and on the windward side of the vehicle with increasing angle of attack. Asymmetric TSM heating occurred on the top surface with changes in model β and on the side surface with changes in model α. Heating extracted at two axial stations on the TSM for the

nominal vehicle reentry case ($\alpha_T = 0°$) was compared with heating for two off-nominal vehicle reentry cases ($\alpha_T = 2°$ and $\alpha_T = 5°$). The maximum heating for the off-nominal reentry cases considered were found to be less than 20% higher than the maximum heating for the nominal reentry case. These data support the JHU/APL thermal analysis of the TSM, which employed a 1.2 factor of safety on the heat transfer coefficient for the $\alpha_T = 0°$ case along with other conservative assumptions. Based on thermal analysis and wind tunnel test results, it was decided by the BOLT team that thermal protection was not necessary on the TSM.

LaRC provided timely feedback on the design of the BOLT vehicle to the flight project, including aeroheating data on the flight geometry, the aerodynamic fairings, and the TSM. The contributions from Langley informed decisions made in the rapid design process for the BOLT flight experiment.

Acknowledgments

Funding for the NASA Langley Research Center contributions to the BOLT project has been provided by the Hypersonics Technology Project. Dr. Bradley Wheaton at JHU/APL provided details of the BOLT TSM thermal analysis. Assistance in model design was completed by Chase Litzner and Richard Wheless. Model fabrication was completed by Robert Andrews, Michael Powers, the LaRC Fab Shop, and the EDM Department (Bartlett, IL). Support for these tests was provided by the NASA Langley 20-Inch Mach 6 Air Tunnel facility technicians and engineers: Johnny Ellis, Kevin Hollingsworth, and Larson Stacy. Data reduction assistance was provided by Carey Scott and Casey Broslawski.

References

[1] Adamczak, D., Alesi, H., and Frost, M., "HIFiRE-1: Payload Design, Manufacture, Ground Test, and Lessons Learned," AIAA 2009-7294, Oct. 2009. doi:10.2514/6.2009-7294.

[2] Kimmel, R., Adamczak, D., Berger, K., and Choudhari, M., "HIFiRE-5 Flight Vehicle Design," AIAA 2010-4985, Jun. 2010. doi:10.2514/6.2010-4985.

[3] Wheaton, B. M., Berridge, D. C., Wolf, T. D., Stevens, R. T., and McGrath, B. E., "Boundary Layer Transition (BOLT) Flight Experiment Overview," AIAA 2018-2892, Jun. 2018. doi:10.2514/6.2018-2892.

[4] Wheaton, B. M., Berridge, D. C., Wolf, T., Araya, D., Stevens, R., McGrath, B. E., Kemp, B., and Adamczak, D., "Final Design of the Boundary Layer Transition (BOLT) Flight Experiment," AIAA 2020-1041, Jan. 2020. doi:10.2514/6.2020-1041.

[5] Berridge, D. C., Kostak, H. E., McKiernan, G. R., Wheaton, B. M., Wolf, T. D., and Schneider, S. P., "Hypersonic Ground Tests With High-Frequency Instrumentation In Support of the Boundary Layer Transition (BOLT) Flight Experiment," AIAA 2019-0090, Jan. 2019. doi:10.2514/6.2019-0090.

[6] Kostak, H. E., Bowersox, R. D., McKiernan, G. R., Thome, J., Candler, G. V., and King, R. A., "Freestream Disturbance

Effects on Boundary Layer Instability and Transition on the AFOSR BOLT Geometry," AIAA 2019-0088, Jan. 2019. doi:10.2514/6.2019-0088.

[7] Berger, K. T., Rufer, S. J., Hollingsworth, K. E., and Wright, S. A., "NASA Langley Aerothermodynamics Laboratory: Hypersonic Testing Capabilities," AIAA 2015-1337, Jan. 2015. doi:10.2514/6.2015-1337.

[8] Buck, G. M., "Rapid Model Fabrication and Testing for Aerospace Vehicles," AIAA 2000-0826, Jan. 2000. doi:10.2514/6.2000-826.

[9] Merski, N. R., "Global Aeroheating Wind-Tunnel Measurements Using Improved Two-Color Phosphor Thermography Method," *Journal of Spacecraft and Rockets*, Vol. 36, No. 2, 1999, pp. 160–170. doi:10.2514/2.3446.

[10] Buck, G. M., "Surface Temperature/Heat Transfer Measurement Using a Quantitative Phosphor Thermography System," AIAA 91-0064, Jan. 1991. doi:10.2514/6.1991-64.

[11] Mason, M. L. and Rufer, S. J., "Features of the Upgraded Imaging for Hypersonic Experimental Aeroheating Testing (IHEAT) Software," AIAA 2016-4322, Jun. 2016. doi:10.2514/6.2016-4322.

[12] Borg, M. P. and Kimmel, R. L., "Simultaneous Infrared and Pressure Measurements of Crossflow Instability Modes for HIFiRE-5," AIAA 2016-0354, Jan. 2016. doi:10.2514/6.2016-0354.

[13] Horvath, T., "Experimental Aerothermodynamics in Support of the Columbia Accident Investigation," AIAA 2004-1387, Jan. 2004. doi:10.2514/6.2004-1387.

[14] Gnoffo, P. A., "An Upwind-Biased, Point-Implicit Relaxation Algorithm for Viscous, Compressible Perfect-Gas Flows," NASA TP-2953, Feb. 1990.

[15] Mazaheri, A., Gnoffo, P. A., Johnston, C. O., and Kleb, W. L., "LAURA Users Manual: 5.5-64987," NASA TM-2013-217800, Feb. 2013.

[16] Roache, P. J., "Perspective: A Method for Uniform Reporting of Grid Refinement Studies," *Journal of Fluids Engineering*, Vol. 116, No. 3, 1994, pp. 405–413. doi:10.1115/1.2910291.

[17] Cheatwood, F. M. and Thompson, R. A., "The Addition of Algebraic Turbulence Modeling to Program LAURA," NASA TM-107758, Apr. 1993.

[18] Berridge, D. C., McKiernan, G., Wadhams, T. P., Holden, M., Wheaton, B. M., Wolf, T. D., and Schneider, S. P., "Hypersonic Ground Tests In Support of the Boundary Layer Transition (BOLT) Flight Experiment," AIAA 2018-2893, Jun. 2018. doi:10.2514/6.2018-2893.